Methods and Applications of Magnetic Induction Tomography: A review

Lu Ma and Manuchehr Soleimani

Engineering Tomography Laboratory (ETL), Department of Electronic and Electrical Engineering, University of Bath, Bath, BA2 7AY, UK

E-mail: L.Ma@bath.ac.uk and M.Soleimani@bath.ac.uk

Abstract. Magnetic induction tomography (MIT) is a tomographic technique capable of imaging the passive electromagnetic properties of an object. It has the advantages of being contact-less and non-invasive, as the process involves interrogating the electromagnetic field of the imaging subject. As such, the potential applications of MIT are broad, with various domains of operation including biomedicine, industrial process tomography and non-destructive evaluation. Consequently, there is a rich – yet underexplored – research landscape for the practical applications of MIT. The aim of this review is to provide a non-exhaustive overview of this landscape. The fundamental principles of MIT are discussed, alongside the instrumentation and techniques necessary to obtain and interpret MIT measurements.

Keywords: magnetic induction tomography, industrial process tomography, non-destructive evaluation, biomedical imaging, eddy current forward problem, MIT inverse problem

1. Introduction

Magnetic induction tomography (MIT) utilises inductive sensing coils to map the electromagnetic properties of an object. As this is a non-intrusive, non-nuclear and contactless technique, it has many potential applications spanning a diverse range of problems and industrial challenges, from biomedical imaging through to non-destructive testing. The development of MIT, in terms of both instrumentation and software, has been given by [1, 2]. A broader overview, covering the theories, systems and potential applications of MIT, was published in [3], as have reviews of specific MIT research advances, such as transmitters and sensors [4]. The aim of this review is to provide an overview of the current research landscape for MIT, discussing the advances, limitations and direction for the future improvement of MIT for three applications: biomedical imaging, industrial process tomography and non-destructive evaluation. To demonstrate how the fundamental theories of MIT can be applied across these differing domains, a generic forward formulation and inverse solver will first be discussed in a step-by-step fashion.

The fundamental principles of MIT can be explained using basic mutual inductance and eddy current theories (Figure 1) [5, 6]. In brief, by passing an alternating current through one or more excitation coils, a primary magnetic field is generated that induces an electric field detectable by one or more measuring coils. From this electric field the induced voltage can then be measured. If a conductive object is placed within this field, an eddy current arises, which can also generate a magnetic field – known as the secondary field. Consequently, the electric field on the measuring coil is induced, in part, by both the primary and secondary fields. The induced voltages on the measuring coil will therefore differ depending on whether a conductive object is present within the field. If no such object is present, the induced voltage arises entirely due to the primary field, whereas if an object is present, the induced voltage arises due to both primary and secondary fields. By analysing the difference in the induced voltages, various properties of the conductive object can be reconstructed.

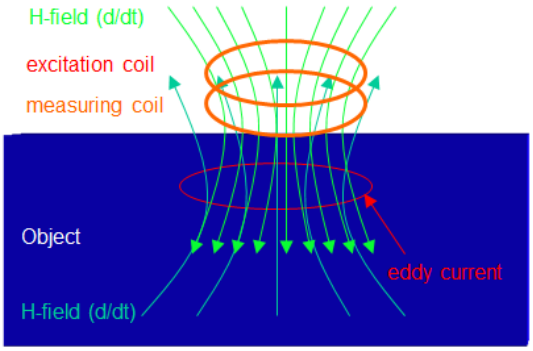

Figure 1. Fundamental principles of MIT.

2. Methods

In MIT, a time-varying current is used in the excitation coil(s) and sensing coils are used to measure the resulting induced voltages. For model-based image reconstruction, the MIT measuring process needs to be simulated, which is called the MIT forward problem. The forward problem is a classic eddy current problem and has been extensively studied in computational electromagnetics using a combination of the magnetic vector potential A, magnetic scalar potential ψ and electric scalar potential ϕ, all of which are fundamentally derived from Maxwell's equations [7, 8, 9, 10]. The eddy current formulation has to comply to both the uniqueness of the fields and the boundary conditions. Difficulties arise when relative boundary conditions are applied, leading to solutions of variable accuracy. For imaging subjects with a simple configuration and a high degree of symmetry, an analytical solution might be applied for linear image reconstruction [11]. However, if the desired image needs to be more realistic, the forward problem cannot be solved this way. For a general solution of the forward problem, the finite element method (FEM) is employed to evaluate the field distribution. This is then used to derive a sensitivity matrix that describes the perturbation in the receiving voltage caused by changes in the electrical properties of the imaging subject [12, 13, 14, 15, 16]. In this article, a (A, A) formulation with edge-finite elements – widely used in MIT forward models – is presented [17].

2.1. Electromagnetic field modelling

In general, the forward problem is solved using full Maxwell's equations. For simplicity, the MIT forward problem can be solved under the condition of a quasi-static electromagnetic field with a few assumptions. First, the displacement current is neglected (when $\sigma >> \omega\varepsilon$); second, the material is considered to have an isotropic character (the effect of material with unisotropical character has been studied in [18]); third, the eddy current effect in the current source is also neglected (when $J_s >> J_e$). Note that there are two regions in the quasi-static electromagnetic field, the non-conducting region and the eddy current region (Figure 2).

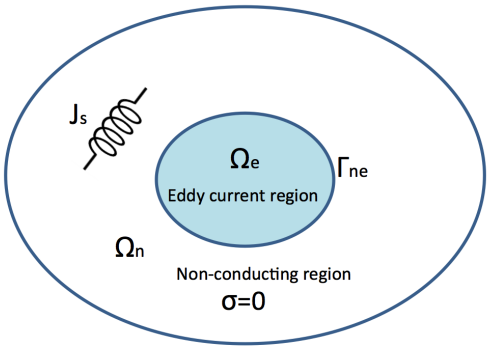

Figure 2. Regions of operation for an MIT system, including a non-conducing region and an eddy current region with an inductive coil located in the proximity.

Using the time-harmonic notation of Maxwell's equations, in the eddy current region Ω_e:

$$\nabla \times H = J_e \tag{1}$$

$$\nabla \times E = -\frac{dB}{dt} \tag{2}$$

$$\nabla \cdot B = 0 \tag{3}$$

In the non-conducting region Ω_n:

$$\nabla \times H = J_s \tag{4}$$

$$\nabla \cdot B = 0 \tag{5}$$

In each region, the B and H fields satisfy that the normal component of the B field is zero and the tangential component of the H field is zero. On the boundary between the two regions Γ_{ne}:

$$B_e \cdot n_e + B_n \cdot n_n = 0 \tag{6}$$

$$H_e \times n_e + H_n \times n_n = 0 \tag{7}$$

where J_e is the eddy current density in Ω_e, J_s is the current density due to the excitation in the non-conducting region Ω_n, n is the normal vector on the boundary, and B_e, H_e, n_e, B_n, H_n, n_n refer to the the magnetic flux, magnetic field and normal vectors in regions of Ω_e and Ω_n respectively. The uniqueness of B and E are therefore ensured.

2.2. Forward model formulation

In the region of $\Omega_n + \Omega_e$ the magnetic field density can be expressed by:

$$\nabla \times H = J_s + \sigma E \tag{8}$$

where J_s is the excitation current source in the coil, which can be prescribed by the magnetic vector potential according to the Biot-Savart Law. E is the induced electric field in the region of $\Omega_n + \Omega_e$, and σ is the conductivity distribution is the eddy current region Ω_e. Note that equation 8 can be extended to include the wave propagation effect, i.e., $\sigma >> \omega\varepsilon$ no longer holds.
Ignoring the displacement current, E can be written in the following form:

$$E = -\frac{\partial A}{\partial t} \tag{9}$$

where the magnetic potential, A, is the sum of two parts: A_s, the magnetic vector potential as result of current source J_s (shown in equation 14), and A_e the reduced magnetic vector potential in the eddy current region Ω_e, and ω is the angular frequency.

$$A = A_s + A_e \tag{10}$$

In the region of Ω_n,

$$\nabla \times H_s = J_s \tag{11}$$

where H_s is the magnetic field generated by an excitation coil in region Ω_n, which can be directly computed from in any point P in free space from J_s:

$$H_s = \int_{\Omega_n} \frac{J_s(Q) \times r_{QP}}{4\pi \mid r_{QP} \mid^3} d\Omega_Q \tag{12}$$

where r_{QP} is the vector pointing from the source point Q to the field point P.

$$\nabla \times A_s = \mu_0 H_s \tag{13}$$

Therefore from equations 11,12 and 13, A_s is readily shown as:

$$A_s = \int_{\Omega_n} \frac{\mu_0 J_s(Q)}{4\pi \mid r_{QP} \mid^2} d\Omega_Q \tag{14}$$

Knowing the permeability μ in the region of Ω_e,

$$H = \frac{1}{\mu} B \tag{15}$$

Combining equations 8, 9, 10, 14, and 15:

$$\nabla \times \frac{1}{\mu} \nabla \times (A_s + A_e) = \nabla \times \frac{1}{\mu_0} \nabla \times A_s - \sigma \frac{\partial (A_s + A_e)}{\partial t} \tag{16}$$

Rearranging equation 16:

$$\begin{aligned} &\frac{1}{\mu} \nabla \times \nabla \times A_e + \sigma \frac{\partial A_e}{\partial t} = \\ &\frac{1}{\mu_0} \nabla \times \nabla \times A_s - \sigma \frac{\partial A_s}{\partial t} - \frac{1}{\mu} \nabla \times \nabla \times A_s \end{aligned} \tag{17}$$

In MIT, the inductive coils are considered magneto-static not antennas; as such the wave propagation effect can be ignored. By approximating the system as a combination of linear equations in small elements with appropriate boundary conditions using edge FEM on a tetrahedral mesh, a vector field is represented using a basis vector function N_{ij} associated with the edge between nodes i and j :

$$N_{ij} = L_i \nabla L_j - L_j \nabla L_i \tag{18}$$

where L_i is a nodal shape function. Applying the edge element basis function to Galerkin's approximation [19, 20, 21, 22], one can obtain:

$$\begin{aligned} &\int_{\Omega_e} (\frac{1}{\mu} \nabla \times N \cdot \nabla \times A_e) dv + \int_{\Omega_e} j\omega\sigma N \cdot A_e dv = \\ &\int_{\Omega_c} (\frac{1}{\mu_0} \nabla \times N \cdot \nabla \times A_s) dv - \int_{\Omega_c} (N \cdot j\omega\sigma A_s) dv - \\ &- \int_{\Omega_c} \nabla \times (N \cdot \frac{1}{\mu} \mu_0 \nabla \times A_s) dv \end{aligned} \tag{19}$$

where N is any linear combination of edge basis functions, Ω_e is the eddy current region, and Ω_c is the coil region. The right hand side in equation 19 can be solved by equations 12 and 14. The only unknown variable is the reduced vector potential A_e. By applying edge FEM, the second order partial differential equations can be computed by a combination of system linear equations, which can then be solved.

The A_e can be obtained using the biconjugate gradients stabilized method to solve the system linear equation [23]:

$$KA_e + MA_e = Jrhs \tag{20}$$

where K and M are the stiffness and math matrices solved by edge FEM, and $Jrhs$ is the right hand side current density.

By solving the reduced magnetic vector potential A_e, one is able to evaluate the induced voltages in the measuring coils. The induced voltages can be calculated by using a volume integration form [24]:

$$V_R = -j\omega \int_{\Omega_c} A \cdot J_0 dv \tag{21}$$

where J_0 is a unit current density following the strands of the receiver coil. Critical to forward modelling is its validation against measured data. Figure 3 shows an example of a forward model validation using an eight-coil MIT system with 28 independent measurements (the detailed system design and application was described elsewhere [25]). The differences between the simulation and experimental data are noticeable. The possible error sources may include the imperfection of the coil geometrical properties, electronic errors, numerical errors such as the effect of the mesh density, and the level of convergence for solving the system linear equation (equation 20). Improvements need to be made in both the modelling software and the sensor design, should a fully non-linear and absolute value MIT imaging be materialised in the future.

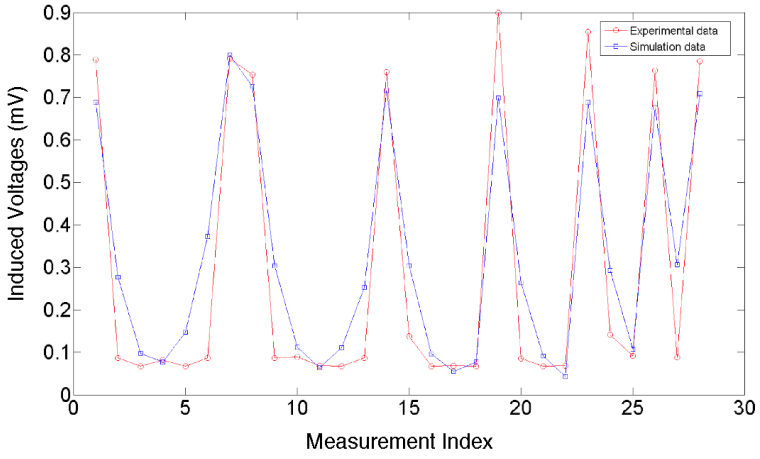

Figure 3. Comparison of simulated voltages and measured voltages for the same given imaging subject.

2.3. Sensitivity formulation

This formulation was derived based on the relationships between the parameters of a test object and its electromagnetic properties, and the extension of Tellegen's theorem to general electromagnetic problems. In this method, a small change in

material property is related to a small change in a physically measured quantity of the electromagnetic fields. In other words a physically measured parameter F is expressed as an integral of the electric E and magnetic H fields over some bounded volume.

$$F = \int_v f(E, H)dv \tag{22}$$

Since the fields are the functions of the system parameters, the variations in F can be approximated with change in system parameters [26].

$$\triangle F = \int_v (S_\sigma \triangle\sigma + S_\mu \triangle\mu + S_\varepsilon \triangle\varepsilon + S_{J_s} \triangle J_s)dv \tag{23}$$

where F is a function of the electric and magnetic fields, J_s is the source current, S represents the sensitivity of the function F to a change in material parameter, and σ, μ and ε are the material electrical conductivity, permeability and permittivity respectively.

The sensitivity distribution is caused by a combination of complex electric field and magnetic field, which are dependent on the configuration of the coils, geometrical and electrical properties of the background, inclusion, as well as the excitation frequency. A detailed derivation of the sensitivity terms for different regimes of measurement (amplitude and phase of the induced voltages) are presented in [27]. Taking the material conductivity as the subject of interest, the sensitivity formulation can be written as equation 24.

$$\frac{\delta V_{mn}}{\delta \sigma_k} = -\frac{\omega^2}{I_m I_n} \int_{\Omega_k} \{A_m\} \cdot \{A_n\} dv \tag{24}$$

where V_{mn} is the induced voltage pairs of coils of m, n with respect to an element, σ_k is the conductivity at element k, Ω_k is the volume of element number k. I_m and I_n are excitation currents for the coil m and coil n, and A_m and A_n are respectively solutions of the forward solver in the eddy currents region (equation 20).

2.4. Image reconstruction algorithm

The inversion of MIT data is an ill-posed inverse problem. As the inverse problem involves inverting the sensitivity matrix, this will make the solution unreliable and sensitive to modelling error and measurement noise. Consequently, a small measurement or modelling error could result in a very large change in the reconstructed conductivity profile. Implementing regularisation techniques that involve introducing additional penalty terms and a smoothing parameter usually mitigates this problem. The inverse problem can usually be formulated in terms of optimising an object function with physical measurements and the goal is to solve the distribution of conductivity (or the other passive electromagnetic properties, formulation here shows electrical conductivity but applies the same ways for other properties) while the measurement signals are given. Solving the inverse problem includes starting with a trial configuration of the system parameters and subsequently modifying this configuration using iterative or non-iterative optimisation algorithms, such as linear back projection [28], Newton one step error reconstruction [29], Tikhonov regularisation (equation 25) [30], Landweber iteration method [31], or the Laplacian regularisation method [32].

The Tikhonov method has been commonly used for time difference MIT image reconstruction to overcome the ill-posedness of the inverse problem. In general,

the algorithm in this problem is formulated as a discrete problem that seeks to minimise the discrepancy between the model and the measured data with respect to the conductivity values in a least squares sense, such that the objective function of the problem is expressed in the generalised Tikhonov form:

$$\sigma^* = argmin_\sigma \left\{ G(\sigma) = \|d(\sigma)\|^2 + \lambda \|L(\sigma - \sigma_{ref})\|^2 \right\} \tag{25}$$

where $\sigma^* \in R^n$ is the discrete solution of the conductivity vector corresponding to n unknown conductivity values $\sigma^* = (\sigma_1, \sigma_2, \sigma_3 \ldots . \sigma_n)^T$ and $d(\sigma) = (F(\sigma) - M) \in R^m$ s the residual between the forward operator $F(\sigma)$ and the measurement data M, σ_{ref} is the user-defined reference conductivity value, and λ and L are the regularisation parameter and regularisation operator matrix respectively. The solution to the problem is found by generating a succession of conductivity vectors $\{\sigma_1, \sigma_2, \sigma_3 \ldots, \sigma^*\}$ that eventually minimise the objective function $G(\sigma)$. Following 25, the Tikhonov method in its iterative form can be expressed as:

$$\triangle\sigma = (J_k^T J_k + \lambda L^T L)^{-1} J_k^T (d(\sigma)) + \lambda L^T L(\sigma_k - \sigma_{ref}) \tag{26}$$

The conductivity profile of the problem domain can then be updated iteratively:

$$\sigma_{k+1} = \sigma_k + \triangle\sigma \tag{27}$$

where k is the number of the iteration and σ_k and J_k are respectively the conductivity and the Jacobian computed on the kth iteration.

3. MIT measurements

3.1. Instrumentation

Regardless of its intended application, a generic MIT system consists of an array of inductive coils, a data acquisition unit (which obtains measurements from these coils), and a host PC for data analysis and image reconstruction. One should note that there is no universal design approach for a MIT system, and that the hardware of a MIT system should be designed to its proposed application. A general consensus – for biomedical applications – is that a suitable MIT system should be able to resolve 1% of the magnetic field perturbation caused by biological tissues [3]. For this application, as the perturbation caused by biological tissues (which have a conductivity range of 0.001S/m to 2S/m) is both very low and proportionate to the driving frequency, then to improve the signal level, frequencies of 1-30MHz have been used to drive the excitation coils. By contrast, for applications of MIT involving metallic structures (such as non-destructive evaluation), the driving frequency of the excitation coils are usually in the range of 5-500kHz.

However, with higher frequency ranges, amplifiers on the receiver coils will in most cases experience degraded performance due to ambient and electronic temperature drift. Consequently, small drifts in the temperature can result in a large drift in the phase measurement, with the phase noise and drift increasing over time as the frequency increases [33]. Amplifiers meeting the requirements of high stability and precision are usually bespoke and often used in military applications, resulting in a much higher cost. Careful selection of the amplifier and subsequent design of the phase detection method are therefore required. Many groups have attempted to increase the signal detectability, such as by adopting a novel zero flow gradiometer design in the MIT receiving circuit to improve spatial sensitivity and reduce the voltage drift and interference from far RF sources [34], and by optimising the receiving coils [35].

Figure 4 shows the Bath biomedical MIT system, comprising an excitation unit, an array of 16 air-cored coils shielded by an aluminium ring, a data acquisition and switching unit, and a host PC for data analysis and image reconstruction.

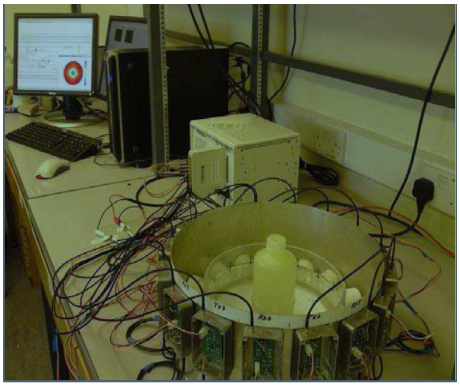

Figure 4. The complete 16 channel MIT system setup for saline bottle detection, adapted from [36] and reproduced courtesy of The Electromagnetics Academy.

3.2. Measurement techniques

The most commonly used MIT phase detection method is in-phase and quadrature (I/Q) demodulation, the implementation of which is often centred on National Instruments (NI) equipment [37]. The I/Q phase demodulation method uses a lock-in amplifier for signal referencing. However, this could compromise the system speed as it takes time to acquire the clock and pass the clock to other channels. Moreover, there is a transient period associated with its use – it takes time for the electronic components to settle. Another drawback of this approach is that data transfer between the NI card and a PC is not particularly fast. This is particularly notable if the switch-acquire-transfer process is completed sequentially, and could limit MIT performance if rapid inspection or real-time imaging is required. Nevertheless, one distinct advantage is that any signal jitter when switching between the receivers could be avoided as all the clocks are synchronised due to the implementation of a phase lock-in method.

A direct phase measurement using heterodyne down-conversion on a transceiver was introduced in [38] and implemented in [39]. This method relies on the fact that the widths of the output signals should remain constant if the phase offset between the received and reference signal pulses remain unchanged. Changes in the width of a pulsed signal reflect phase changes due to the perturbation of the imaging subject in the electromagnetic field, and can be measured directly using an oscilloscope with a counter. More in-depth evaluation of the phase noise caused by the down-conversion of these direct measurements was studied in [40]. One potential problem associated with this method is the phase skew induced by a low signal amplitude.

Another direct phase measurement is the use of the Fast Fourier Transform algorithm to measure the phase [41]. This method has the advantage of being fast and particularly useful for multi-frequency signals. It was shown in [42] that for frequencies ranging from 0.5-14MHz, a phase noise lower that 1millidegree is possible. In addition, it was found that over a 12 hour period of phase measurement, the reported phase

drift was lower than 20 millidegrees. Nevertheless, problems can arise with FTT in the form of spectral leakage, which can occur if the received signal does not contain an exact number of cycles. This is usually the case for a real-time signal. Good practice to avoid spectral leakage is to ensure the sample length is in the same range as the resolution of the signal synthesizer.

3.3. Multi-frequency operation

The detectability and imaging capability of MIT could be improved using multi-frequency excitations. This is based on the fundamental principle that conductivity is frequency-dependent. High frequency measurements give information regarding the properties adjacent to the surface of the imaging subject, whereas low frequency measurements probe deeper inside it. The major challenges of implementing multi-frequency MIT are in conditioning electronics and software control. In [43], the hardware electronics and software control were studied to facilitate the implementation of three sinusoidal signals with target frequencies below 1kHz for simultaneous excitation. This multi-frequency system was proposed for the visualisation of steel flows. As for non-magnetic, electrically conductive metals – i.e., when $\mu_r = 1$ – a single frequency might meet the skin depth requirement. However, for other materials such as steel, where both conductivity and permeability play important roles, using a single selected frequency would not be sufficient to accurately reconstruct an image differentiating different steel flow profiles. Hardware development of multifrequency systems have also been studied for imaging biological tissues, where in [44] the system employed ten excitation frequencies between 40 and 370kHz and the multi-frequency measurements were made using planar gradiometers; while in [45] the multi-frequency MIT system employed a higher frequency range from 50kHz to 1MHz, the detailed data collection and calibration on this system were also presented. Therefore it is desirable to design an excitation channel to provide a range of excitation frequencies suitable for the imaging target as this could increase the information available to an MIT system, making reconstructed images more robust to anomalies.

Enhancing the MIT software to be able to collect multi-frequency data, alongside reconstructing spectral and frequency differences, is particularly useful for imaging conductive materials with anisotropic characteristics [18]. Of additional interest is frequency difference imaging, which could be useful if the test subjects show different responses to frequency variation. The reconstruction of pathophysiological information using multi-frequency data and frequency dependence sensitivity matrix was studied in [46], which showed that low resolution similar to those obtained from electrical impedance tomography is possible.

4. Applications

4.1. Biomedical imaging

Developing an accurate biomedical imaging device for low-cost real time monitoring would offer considerable diagnostic advantages, particularly when early detection strongly influences prognosis – for instance, in the case of brain haemorrhage or cerebral stroke. The most commonly used imaging techniques, X-ray computed tomography and magnetic resonance imaging (MRI), are comparatively expensive. In addition, the diagnostic process may involve hazardous radiation and therefore

cannot be applied to all patients. As such, MIT has attracted interest as an alternative technique. However, as biological tissues usually have conductivity lower than 2S/m, then in order to account for any field perturbation, a phase change of 1 millidegree needs to be resolved [3]. This is challenging from the perspective of system design.

The first application of MIT to biomedical imaging demonstrated that 0.1 and 0.01 mole/l NaCl concentrations (equivalent conductivity of 1S/m and 0.1S/m) in deionized water (which approximate fat-free and fat-rich tissue conductivities) can be distinguished [47]. In addition to this experimental work, simulations have been made of a range of biological tissues, including the spine (0.007S/m), lungs (0.05S/m), skeletal muscle (0.1S/m) and heart (0.5S/m) [38], and of a specific condition, hemorrhagic stroke, using a 16-channel system operating at 10MHz [48]. In [49], a single channel MIT system measured conductivity from 0.001S/m to 6S/m, encompassing an even greater range of biological tissues including high water content tissue (this work also validated a theoretical prediction that the induced magnetic field is proportional to the conductivity). A full MIT system was later developed to carry out phantom-based biomedical imaging [50], which could detect a conducting tube of average conductivity 0.2S/m at 6cm from the sensor [51]. Imaging results were shown in [52] for conductivity ranging from 0.27S/m to 0.50S/m – equivalent to that of a human thigh (depending on the body mass index). The first conductivity image of a leech was presented in [53]; the location and the shape of the leech could be identified through the reconstructed images.

We have also investigated the feasibility of cryosurgical monitoring using the MIT system shown in Figure 4 [54]. The imaging region is formed by 16 equally spaced air-cored sensors; each has 6 turns, a side length of 1cm, and a radius of 2cm. The radius of the imaging region is 12cm. Among 16 coils, 8 coils are engaged for transmitting signals, and the other 8 coils are dedicated for receiving signals; the total number of independent measurement is therefore 64. The driving frequency of this system is 13MHz. The imaging region was filled with a fluid with an electrical conductivity of 0.9S/m, similar to that of the saline conductivity used in clinical treatment. Four different sized insulating bottles (of diameters 2cm, 6.5cm, 9.5 cm and 13cm) are used to represent frozen areas, i.e., the area undergoing cryosurgical treatment. Reconstructed images of the frozen areas are shown in Figure 5 and 6. The reconstructed images are presented in such a manner that red color shows the background conductive fluid, and all other colors show the area occupied by the insulting bottle.

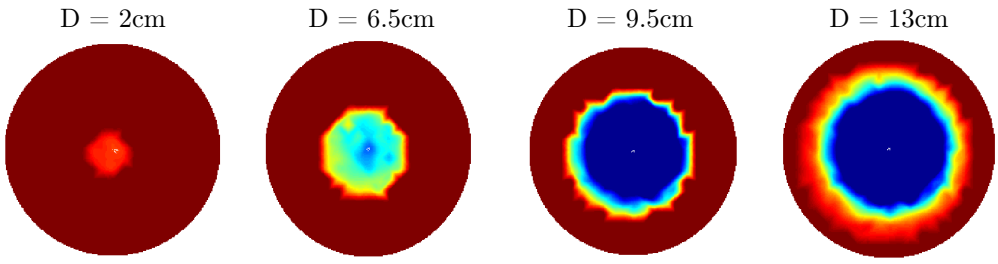

Figure 5. Reconstructed images of non-conductive imaging subjects (differently sized insulated bottles) located in the centre of a saline background with a conductivity of 0.9S/m.

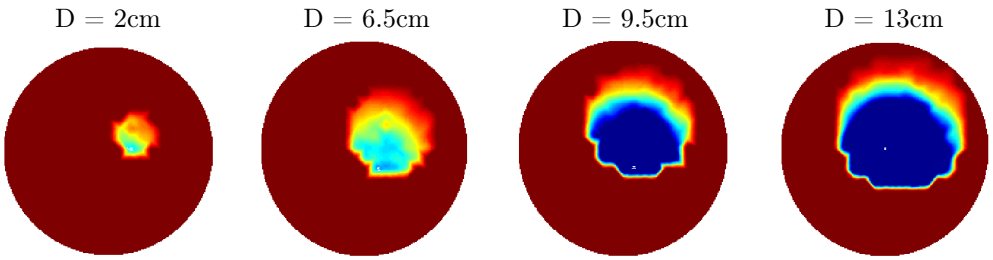

Figure 6. Reconstructed images of non-conductive imaging subjects (differently sized insulated bottles) located off the centre against a saline background with a conductivity of 0.9S/m.

4.2. Industrial process tomography

In the steel industry, an 8-coil MIT system operating at 5kHz was proposed for the visualisation of metal flows [55]. Laboratory phantom tests were conducted to represent several typical metal flow profiles such as central, annular stream and multiple streams using metal rods. The MIT system used for this application claimed to have a frame rate of 10 frames/s, which enabled real-time logging of the process data and online image update. Effort has also been made to image molten flow passing through a submerged entry nozzle using this system, with hot trial results consistent with simulations [43]. In addition, in this paper, the authors also presented a multi-frequency approach to identify a range of samples, which could improve the imaging capability of MIT for a complex metal flow. Taken together, this is an encouraging step forward for the commercial development of MIT.

In recent years, MIT has also been used to visualise the conducting phase of a multiphase flow. MIT is considered more advantageous for flow imaging compared to electrical resistance tomography techniques [56, 57, 58]. However, due to the low resolution of MIT, the realisation of this technique as a smart imaging device for industrial process tomography remains a challenging topic, with the experimental validation of two-phase and multi-phase flow imaging still limited. Nevertheless, MIT could be complementary to existing techniques for multi-phase flow imaging as it is sensitive to the conductive component of the flow mixtures [59]. A single channel MIT system has been used to measure the water content in multi-phase flow using experimental phantom recordings. It was found that the correlation between the position of the coil and the water/oil interface could be overcome by a full tomographic system [60] (a similar conclusion has also been drawn in [61]).

In an attempt to image conductive or ferromagnetic properties in two phase flow, a parallel excitation structure for MIT was shown in [62]. However, this work was limited in scope, focusing on the simulation of the sensing field only, and as such experimental results were not included. It was not until 2008 that a full MIT system had demonstrable feasibility for two phase flow imaging. A phantom simulated multi-phase flow in an oil pipeline with a system speed of 90s per frame was carried out in [52]. More recently, experimentally-derived two phase flow images were demonstrated in [36] using a 16 channel MIT system (Figure 4), showing that a conductivity contrast as small as 1.58S/m can be imaged. A further evaluation of the distribution of air

bubbles in a two phase flow using quasi-static experimental data was given in [63]. A stream of bubble gas was injected on the periphery of the flow rig at 2 points opposite each other to introduce the perturbation to the electromagnetic field (Figure 7). The background fluid has a conductivity of 5.13S/m, similar to that of the produced water. A snap shot of the bubble testing is reconstructed to show the average bubbles along the axial direction (Figure 8). Promising results have also demonstrated how MIT could aid electrical capacitance tomography (ECT) to image a mixture of conductive and dielectric materials [64]. The further development of MIT-based multi-modality tomography could therefore be applicable to various industrial processes.

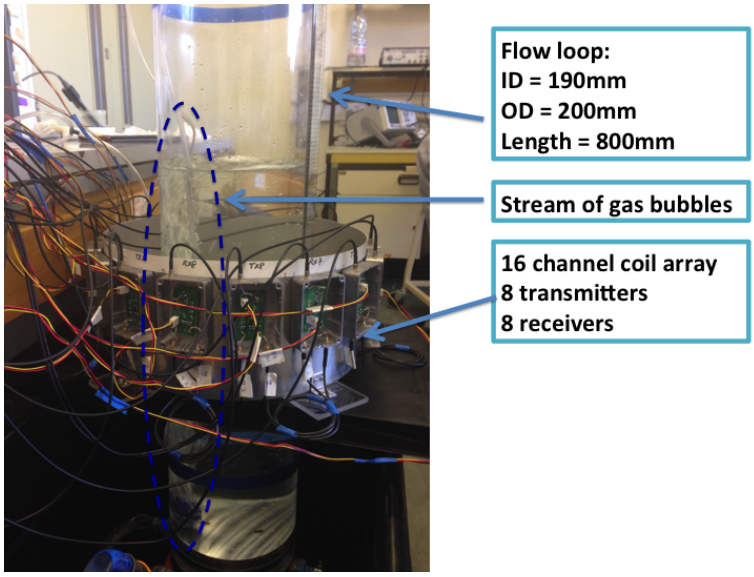

Figure 7. Bubble testing setup, adapted from [63] and reprinted with permission from Elsevier.

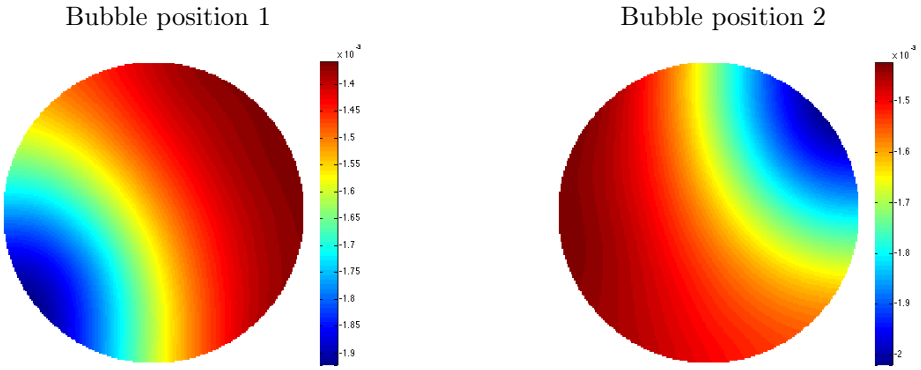

Figure 8. Reconstructed images of bubble flow in a background fluid with a conductivity of 5.13S/m. Adapted from [63] and reprinted with permission from Elsevier.

4.3. Non-destructive evaluation

Non-destructive evaluation (NDE) is vital to public safety and an intrinsically interdisciplinary field, using multiple techniques to inspect the structural integrity of a subject. Many studies have been published to demonstrate the promise of MIT in this industry. The earliest concept of using MIT for non-destructive evaluation was proposed in 1985, to inspect airplane wings for cracks after continued flexing of their structure [65]. This work was largely theoretical, although a scanning rig and an analogue device for one transducer was designed was designed to reconstruct magnetic vector potential (but not the conductivity distribution).

In general, MIT offers the considerable benefit of being non-invasive: there is no requirement for direct contact with the material being tested, such as with gels (various ultrasonic methods), specially designed probes (injected current thermography) or electrodes attached to the composite parts (electrical impedance tomography, EIT). In addition, by using electromagnetic induction to map the spatial resolution, MIT has a non-hazardous data collection process. When compared to X-ray computed tomography, for instance, radiation safety precautions need to be considered, which can in certain circumstances be impractical. MIT also has a high temporal resolution although compared to other techniques its image resolution is comparatively low: MIT image reconstruction is an ill-posed problem. More recently, rapid changes in electrical conductivity were captured using MIT alongside Kalman filters and 4D temporally correlated imaging [66, 67]. This would potentially enable functional analysis of the testing structures, of particular interest because this is not currently feasible with any other existing technique.

Eddy current testing is arguably the most established method in non-destructive evaluation, although it was not until the 1980s that this technique was fully exploited. In a general sense, both MIT and eddy current testing techniques share many similarities – both arose from the same theoretical background (that of Faraday's law of induction, and subsequent eddy current theories) and so have similar measurement principles, and both are used to image conductive or ferromagnetic materials. Nevertheless, the techniques differ both in their methods of data processing and their operation (with eddy current testing usually requiring a certified specialist to

perform). MIT is a tomographic approach and in general more robust, utilising an array of sensors to create a vector of amplitudes or phase angles from the induced voltages, whereas eddy current imaging maps the distribution of the defect within a localised position using a pair of coils. Decreased electrical potential across these coils is a measure of their impedance, with impedance related to the location and size of the defect.

In [68], MIT was also proposed for industrial pipeline inspection. As MIT coils are relatively low cost either to make or purchase, coil arrays can be designed for a particular application. If access is restricted and non-invasive measurements can only be taken from one surface, planar MIT is a viable solution. A simulation study of planar MIT was reported in [69], where 2D cross-sectional images of conductive bars were obtained using an iterative simultaneous increment reconstruction technique. In [70], a planar MIT system for detecting conductivity inhomogeneity on the surface of a metallic plate was presented. The experimental realisation of planar MIT has also been extended to 3D subsurface imaging, where aluminium rods can be inspected at distances of 3-4cm beneath the planar array [71].

In addition to inspecting metallic materials, MIT has also been developed to inspect carbon fiber reinforced polymer (CFRP), a material with widespread application in commercial aircraft, industrial and transportation markets, where strength, stiffness, a lower weight, and outstanding fatigue characteristics are crucial requirements. As the carbon fibres in CFRPs exhibit electrical conductivity, MIT could be a potential NDE technique providing a tomographic approach to traditional eddy current testing. This was verified in [72] where damages in carbon fiber-reinforced plastics were experimentally investigated. Another 3D experimental study has also demonstrated that images of one or more hidden defects inside CFRPs can be reconstructed, although differences in defect size (15 and 25mm diameter holes within CFRP layers) could not be distinguished [73]. Despite the encouraging results, it is clear that the CFRP samples included in these studies are not sufficiently representative to cover all possible manufacturing defects or impact damage which may occur in a real industrial environment. For example, impact damage could alter electrical conductivity to a point where conductivity changes are not as high contrast (and therefore visualisable) as those shown in previous work. Furthermore, some CFRPs could have anisotropic characteristics, requiring the forward problem be modelled and solved with a high degree of accuracy [74, 75].

5. Discussion

The primary difficulty in applying MIT to biomedical imaging is forward modelling. This is because the sensitivity map (of a conductive inclusion in a free space) is dependent on conductivity contrasts, which might be invalid for biological tissues. Simulations have showed that slight distortions of the receivers could result in 20% deviations to the conductivity perturbation [76]. Even with more accurate sensor modelling, the imaging process can still be demanding, as slight movements of the human body (which, for a conscious patient, are inevitable) could corrupt valuable information and result in artifacts in the reconstructed image [77]. As such, a full eddy current problem not only needs to be solved but updated in an iterative fashion [16]; this could significantly increase the computational cost. This cost would increase still further if the forward model is very dense, such as the millions of elements necessary for brain imaging.

Furthermore, for a 2D problem, the inverse solver can usually be handled by a central processing unit (CPU), but for a 3D problem (or any problem with a large number of voxels), this could be inefficient for the solving process. High performance computing techniques using graphics processing units (GPUs) have been proposed to address this, where the parallelisation scheme was implemented on both the forward and inverse solver [78, 79, 80], significantly reducing computational time.

Although online health monitoring using MIT has yet to be deployed in clinical trials, it is nevertheless an imaging technique with great promise. To be realistically possible, however, any potential clinical application should allow for MIT data collection over time, i.e., so that physiological or functional changes can be monitored.

It is common practice to use phantom simulated data to study the feasibility and capability of MIT both in biomedical imaging and industrial process tomography. This is because it is easy to develop phantoms of different sizes, shapes, and conductivities at relatively low cost, and to keep the conductivity distribution of the phantoms both uniform and free from contamination for a lengthy period. In this respect, simulation results can easily be validated against experimental data. However, the scope of phantom-based studies is limited in that the experiments are often conducted in static or quasi-static conditions with limited frame rate (that is, real-time data is usually absent). For example, if accurately imaging a flow of average speed 5m/s, an average of 20 measurements need to be taken per second (using a commercial capacitance tomography system as a benchmark [81]). This would require a system with a frame rate no less than 100 frames per second. At present, however, there is no known MIT system operating at such frame rate. Although methods to improve the system frame rate have been articulated [82], it will likely be some time before the standards of a commercial system can be met – with phantom-based studies unsuited to testing the feasibility of new developments. In addition, the primary focus of phantom studies is often imaging the conductivity distribution – the derivation of process parameters from the MIT measurements, also of interest to industrial end-users, are not covered.

6. Conclusions

This paper presents an overview of a number of potential applications of MIT and provides evidential basis for the future exploitation of MIT. The two major challenges for future development are hardware development, so as to meet the standards of widespread commercial applications, and increasing software capability to allow for fully automated real-time image reconstruction and structural analysis of the imaging subject. In our opinion, successful applications of MIT require an imaging algorithm with an experimentally verifiable forward model and high-speed hardware capable of producing repeatable and stable measurements. In this respect, it is recommended that a number of benchmark MIT tests should be developed and adapted by the research community for the process of validation of their forward and inverse models. It is hoped that MIT could eventually be commercialised as, for instance, a rapid NDE system or a 24/7 health monitoring system, thereby contributing both to the social economy and public good.

Acknowledgments

Figure 6 is reprinted from Progress In Electromagnetics Research, Vol. 131, H. - Y. Wei and M. Soleimani, Two-phase low conductivity flow imaging using magnetic induction tomography, Pages No.99–115., Copyright (2012), with permission from the The Electromagnetics Academy.
Figure 9 and 10 are reprinted from The International Journal of Multiphase Flow, Vol. 72, L. Ma, A. Hunt and M. Soleimani, Experimental Evaluation of Conductive Flow Imaging Using Magnetic Induction Tomography, Pages No.198-209., Copyright (2015), with permission from Elsevier.

References

[1] A. J. Peyton, M. S. Beck, A. R. Borges, J. E. de. Oliveira, G. M. Lyon, Z. Z. Yu, M. W. Brown, and J. Ferrerra. Development of electromagnetic tomography (emt) for industrial applications. part 1: sensor design and instrumentation. In *1st World Congress on Industrial Process Tomography*, pages 306–312, Buxton, UK, 14-17 April 1999.

[2] A. R. Borges, J. E. de. Oliveira, J. Velez, F. Linhares, and A. J. Pe. Development of electromagnetic tomography (emt) for industrial aapplication. part 2: Image reconstruction and software framework. In *1st World Congress on Industrial Porcess Tomography*, pages 14–17, Buxton, April 1999.

[3] H. Griffiths. Magnetic induction tomography. *Measurement Science and Technology*, 12:1126–1131, 2001.

[4] Z. Zakaria, R. A. Rahim, M. S. B. Mansor, S. Yaacob, N. M. N. Ayob, S. Z. M. Muji, M. H. F. Rahiman, and S. M. K. S. Aman. Advancements in transmitters and sensors for biological tissue imaging in magnetic induction tomography. *Sensors Review*, 12:7126–7156, 2012.

[5] Z. Z. Yu, A. J. Peyton, W. F. Conway, L. A. Xu, and M. S. Beck. Imaging system based on electromagnetic tomography (emt). *Electronics Letters*, 29(7):625–626, 1993.

[6] G. M. Lyon, Z. Z. Yu, A. J. Peyton, and M. S. Beck. Developments in electro-magnetic tomography instrumentation. In *IEE Colloquium on Advances in Electrical Tomography (Digest No: 1196/143)*, volume 12, pages 1–4, June 1996.

[7] An edge finite element eddy current formulation using a reduced magnetic and a current vector potential. *IEEE Transactions on Magnetics*, 36(5):3128–3130, 2000.

[8] A. Kameari. Three dimensional eddy current calculation using edge element for magnetic vector potential. *International Journal of Applied Electromagnetics and Mechanics*, pages 225–236, 1986.

[9] W. Renhart, H. Stogner, and K. Preis. Calculation of 3d eddy current problems by finite element method using either an electric or a magnetic vector potential. *IEEE Transactions on Magnetics*, 24(1):122–125, 1988.

[10] R. Albanese and G. Rubinacci. Solution of three dimensional eddy-current problems by integral and differential methods. *IEEE Transactions on Magnetics*, 24(1):98–101, 1988.

[11] W. L. Yin, S. J. Dickinson, and A. J. Peyton. Imaging the continuous conductivity profile within laryerd metal structures using inductance spectroscopy. *IEEE Sensors*, 5:161–166, 2005.

[12] R. Merwa, K. Hollaus, B. Brandstatter, and H. Scharfetter. Numerical solution of the general 3d eddy current problem for magnetic induction tomography (spectroscopy). *Physiological Measurement*, 24(2):545–554, 2003.

[13] M. N. Tek and N. G. Gençer. A new 3d fem formulation for the solution of potential fields in magnetic induction problems. In *Engineering in Medicine and Biology Society, 1997. Proceedings of the 19th Annual International Conference of the IEEE*, volume 6, pages 2470–2473, 1997.

[14] N. G. Gençer and M. N. Tek. Forward problem solution for electrical conductivity imaging via contactless measurements. *Measurement Science and Technology*, 44:927–940, 1999.

[15] N. G. Gençer and M. N. Tek. Electrical conductivity imaging via contactless measurments. *IEEE Transactions on Medical Imaging*, 18(7):617–627, 1999.

[16] H. Scharfetter, P. Riu, M. Populo, and J. Rosell. Sensitivity maps for low-contrast perturbations within conducting background in magnetic induction tomography. *Physiological Measurement*, 23(1):195–202, 2002.

[17] M. Soleimani, W. Lionheart, C. Riedel, and O. Dossel. Forward problem in 3d magnetic induction tomography (mit). In *Proceedings of the 3rd World Congress on Industrial Process Tomography*, Banff, Alberta., 2003-09-02 - 2003-09-05 2003.

[18] D. Gürsoy and H. Scharfetter. Anisotropic conductivity tensor imaging using magnetic induction tomography. *Physiological Measurement*, 31(8):S135–S145, 2010.

[19] D. C. Barber and B. H. Brown. Applied potential tomography. *Journal of Physics E: Scientific Instruments*, 17(9):723–734, 1984.

[20] N. A. Golias, C. S. Antonopoulos, T. D. Tsiboukis, and E. E. Kriezis. 3d eddy current computation with edge elements in terms of the electric intensity. *The International Journal for Computation and Mathematics in Electrical and Electronic Engineering*, 17(5/6):667–673, 1998.

[21] V. Thomée. *Galerkin Finite Element Methods for Parabolic Problems*, volume 25. Springer Series in Computational Mathematics, 2nd ed edition, 2006.

[22] B. Rivière. *Discontinuous Galerkin methods for solving elliptic and parabolic equations: theory and implementation*. Society for Industrial and Applied Mathematics, 2008.

[23] H. Igarashi and T. Honma. On convergence of iccg applied to finite-element equation for quasi-static fields. *IEEE Transactions on Magnetics*, 38(2):565–568, 2002.

[24] C. Ktistis, D. W. Armitage, and A. J. Peyton. Calculation of the forward problem for absolute image reconstruction in mit. *Physiological Measurement*, 29:S455–S464, 2008.

[25] L. Ma and M. Soleimani. Electromagnetic imaging for internal and external inspection of metallic pipes. *Insight-Non-Destructive Testing and Condition Monitoring*, 54(9):493–495, 2012.

[26] D. N. Dyck, D. A. Lowther, and E. M. Freeman. A method of computing the sensitivity of the electromagnetic quantities to changes in the material and sources. *IEEE Transactions on Magnetics*, 30:3415–3418, 1994.

[27] W. R. B. Lionheart, M. Soleimani, and A. J. Peyton. Sensitivity analysis in 3d magnetic induction tomography. In *Proceedings 3rd World Congress on Industrial Process Tomography*, pages 239–244, Canada, 2003.

[28] W. Q. Yang and L. H. Peng. Image reconstruction algorithms for electrical capacitance tomography. *Measurement Science and Technology*, 14(1):R1–R13, 2003.

[29] H. Scharfetter, K. Hollaus, J. Rosell, and R. Merwa. Single step 3-d image reconstruction in magnetic induction tomography: theoretical limits of spatial resolution and contrast to noise ratio. *Annals of Biomedical Engineering*, 34:1786–1798, 2006.

[30] M. Ziolkowski, S. Gratkowski, and R. Palka. Solution of three dimensional inverse problem of magnetic induction tomography using tikhonov regularization method. *International Journal of Applied Electromagnetics and Mechanics*, 30(3 - 4):245–253, 2009.

[31] W. Q. Yang, D. M. Spink, T. A. York, and H. McCann. An image-reconstruction algorithm based on landweber's iteration method for electrical-capacitance tomography. *Measurement Science and Technology*, 10(11):1065–1069, 1999.

[32] B. Brandstatter, G. Holler, and D. Watzenig. Reconstruction of inhomogeneities in fluids by means of capacitance tomography. *COMPEL: The International Jounal for Computation and Mathematics in Electrical and Electronic Engineering*, 22(3):508–519, 2003.

[33] S. Watson, H. C. Wee, H. Griffiths, and R. J. Williams. A highly phase-stable differential detector amplifier for magnetic induction tomography. *Physiological Measurement*, 32(7):917, 2011.

[34] H. Scharfetter, R. Merwa, and K. Pilz. A new type of gradiometer for the receiving circuit of magnetic induction tomography (mit). *Physiological Measurement*, 26(2):S307–S318, 2005.

[35] D. Gürsoy and H. Scharfetter. Optimum receiver array design for magnetic induction tomography. *IEEE Transactions on Biomedical Engineering*, 56(5):1435–1441, 2009.

[36] H. Y. Wei and M. Soleimani. Two-phase low conductivity flow imaging using magnetic induction tomography. *Progress In Electromagnetics Research*, 131:97–115, 2012.

[37] H.-Y. Wei and M. Soleimani. Hardware and software design for a national instrument-based magnetic induction tomography system for prospective biomedical applications. *Physiological Measurement*, 33(5):863–879, 2012.

[38] A. V. Korzhenevsky and V. A. Cherepenin. Progress in realization of magnetic induction tomograph. *Annals of the New York Academy of Sciences*, 873:346–352, 1999.

[39] S. Watson, R. J. Williams, H. Griffiths, W. Gough, and A. Morris. A transceiver for direct phase measurement magnetic induction tomography. In *Engineering in Medicine and Biology Society. Proceedings of the 23rd Annual International Conference of the IEEE*, volume 4, pages 3182–3184, 2001.

[40] S. Watson, R. J. Williams, H. Griffiths, W. Gough, and A. Morris. Frequency downconversion and phase noise in mit. *Physiological Measurement*, 23:189–194, 2002.

[41] R. Patz, S. Watson, C. Ktistis, M. Hamsch, and A. J. Peyton. Performance of a fpga-based direct digitising signal measurement module for mit. In *International Conference on Electrical Bioimpedance, Journal of Physics: Conference Series 224*, number 1, 2010.

[42] H. C. Wee, S. Watson, R. Patz, H. Griffiths, and R. J. Williams. A magnetic induction tomography system with sub-millidegree phase noise and high long-term phase stability. In *4th European Conference of the International Federation for Medical and Biological Engineering*, volume 22 of *IFMBE Proceedings*, pages 744–747. Springer Berlin Heidelberg, 2009.

[43] X. Ma, A. J. Peyton, S. R. Higson, and P. Drake. Development of multiple frequency electromagnetic induction systems for steel flow visualization. *Measurement Science and Technology*, 19(9):094008, 2008.

[44] H. Scharfetter, H. K. Lackner, and J. Rosell. Magnetic induction tomography: hardware for multi-frequency in biological tissue. *Physiological Measurement*, 22(1):131–146, 2001.

[45] J. Rosell-Ferrer, R. Merwa, P. Brunner, and H. Scharfetter. A multifrequency magnetic induction tomography system using planar gradiometers: data collection and calibration. *Physiological Measurement*, 27:S271–S280, 2006.

[46] P. Brunner, R. Merwa, A. Missner, J. Rosell, K. Hollaus, and H. Scharfetter. Reconstruction of the shape of conductivity spectra using differential multi-frequency magnetic induction tomography. *Physiological measurement*, 27:S237–S248, 2006.

[47] S. AL-Zeibak and N. H. Saunders. A feasible study of in vivo electromagnetic imaging. *Physics in Medicine and Biology*, 38:151–160, 1993.

[48] Y. N. Chen, M. Yan, D. Chen, M. Hamsch, H. Liu, H. Jin, M. Vauhkonen, C. H. Igney, J. Kahlert, and Y. Y. Wang. Imaging hemorrhagic stroke with magnetic induction tomography: realistic simulation and evaluation. *Measurement Science and Technology*, 21:809–827, 2010.

[49] H. Griffiths, W. R. Stewart, and W. Gough. Magnetic induction tomography: a measuring system for biological tissues. *Annals of the New York Academy of Sciences*, 873:335–345, 1999.

[50] A. V. Korjenevsky, V. A. Cherepenin, and S. Sapetsky. Magnetic induction tomography: experimental realization. *Physiological Measurement*, 21(1):89, 2000.

[51] B. Ü. Karbeyaz and N. G. Gençer. Electrical conductivity imaging via contactless measurements: an experimental study. *IEEE Transactions on Medical Imaging*, 22:627–635, 2003.

[52] S. Watson, R. J. Williams, W. Gough, and H. Griffiths. A magnetic induction tomography system for samples with conductivities below 10s/m. *Measurement Science and Technology*, 19(4):045501, 2008.

[53] K. Ö. Özkan and N. G. Gençer. Low-frequency magnetic subsurface imaging: Reconstructing conductivity images of biological tissues via magnetic measurements. *IEEE Transactions on Medical Imaging*, 28(4):564–570, 2009.

[54] L. Ma, H.-Y. Wei, and M. Soleimani. Cryosurgical monitoring using electromagnetic measurements: A feasibility study for magnetic induction tomography. In *13th International Conference in Electrical Impedance Tomography*, Tianjin University, Tianjin., 2012-05-23 - 2012-05-25 2012.

[55] X. Ma, A. J. Peyton, S. R. Higson, A. Lyons, and S. J. Dickinson. Hardware and software design for an electromagnetic induction tomography (emt) system for high contrast metal process applications. *Measurement Science and Technology*, 17(1):111–118, 2006.

[56] H. Jin, Y. Lian, S. Yang, G. He, and G. Guo. The parameters measurement of air-water two phase flow using the electrical resistance tomography (ert) technique in a bubble column. *Special Issue IWPT-4 in Flow Measurement and Instrumentation*, 31:55–60, 2013.

[57] L. Su, Z.-P. Song, B.-S. Wang, and L. Ding. Research on void fraction of gas-liquid two-phase flow based on comsol and matlab. *Journal of Ship Mechanics*, 17(5):460–467, 2013.

[58] J. Zhang and F. Ma. Application of electrical resistance tomography to ice-water two-phase flow parameters measurement. *Key Engineering Materials*, 562-565:686–690, 2013.

[59] R. Thorn, G. A. Johansen, and B. T. Hjertaker. Three-phase flow measurement in the petroleum industry. *Measurement Science and Technology*, 24:012003, 2013.

[60] R. A. Albrechtsen, Z. Z. Yu, and A. J. Peyton. Preliminary experiments on the investigation of the inductive technique for measuring water content in multiphase flow. In *Proc. ECAPT*, pages 205–213, Bergen, 1995.

[61] E. A. Hammer and G. Fossdal. A new water-in-oil monitor based on high frequency magnetic field excitation. In *Proceedings of the 2nd international symposium on process tomography*, pages 9–16, Wroclaw, Poland, 2002.

[62] Z. Liu, M. He, and H.-L. Xiong. Simulation study of the sensing field in electromagnetic tomography for two-phase flow measurement. *Flow Measurement and Instrumentation*, 16(2):199 – 204, 2005.

[63] L. Ma, A. Hunt, and M. Soleimani. Experimental evaluation of conductive flow imaging using magnetic induction tomography. *International Journal of Multiphase Flow*, 72:198–209, 2015.

[64] M. Zhang, L. Ma, and M. Soleimani. Dual modality mit-ect multi-phase flow imaging. *Flow Measurement and Instrumentation*, 46:240–254, 2015.

[65] D. J. Kyte. *Magnetic Induction Tomography and Tchniques for Eddy-Current Imaging*. PhD thesis, University of Surrey, 1985.

[66] M. Soleimani. Improving the temporal resolution of magnetic induction tomography for molten metal flow visualization. *IEEE Transactions on Instrumentation and Measurement*, 59(3):553–557, 2010.

[67] H. Y. Wei and M. Soleimani. Four dimensional reconstruction using magnetic induction tomography: experimental study. *Progress In Electromagnetics Research*, 129:17–32, 2012.

[68] L. Ma, H. Y. Wei, and M. Soleimani. Pipeline inspection using magnetic induction tomography based on a narrowband pass filtering method. *Progress In Electromagnetics Research M*, 23:65–78, 2012.

[69] S. Ramli and A. J. Peyton. Feasibility study of planar-array electromagnetic inductance tomography (emt). In *1st World Congress on Industrial Process Tomography*, Buxton, Greater Manchester, April 14-17 1999.

[70] W. Yin and A. J. Peyton. A planar emt system for the detection of faults on thin metallic plates. *Physiological Measurement*, 17(8):2130–2135, 2006.

[71] L. Ma, H.-Y. Wei, and M. Soleimani. Planar magnetic induction tomography for 3d near subsurface imaging. *Progress In Electromagnetics Research*, 138:65–82, 2013.

[72] A. Renner, W.-J. Fischer, and U. Marschner. A new imaging approach for in-situ and ex-situ inspections of conductive fiber reinforced composites by magnetic induction tomography (mit). *Journal of Intelligent Material Systems and Structures*, 25(9):1149–1162, 2013.

[73] L. Ma and M. Soleimani. Hidden defect identification in carbon fibre reinforced polymer plates using magnetic induction tomography. *Measurement Science and Technology*, 25(5):055404, 2014.

[74] M. D. V. Hari Kishore, B. N. Singh, and M. K. Panditbr. Nonlinear static analysis of smart laminated composite plate. *Aerospace Science and Technology*, 15(3):224–235, 2011.

[75] B. M. Kolundzija. Electromagnetic modeling of composite metallic and dielectric structures. *IEEE Transactions on Microwave Theory and Techniques*, 47:1021–1032, 1999.

[76] D. Gürsoy and H. Scharfetter. Imaging artifacts in magnetic induction tomography caused by the structural incorrectness of the sensor model. *Measurement Science and Technology*, 22(1):015502, 2011.

[77] D. Gürsoy and H. Scharfetter. Reconstruction artefacts in magnetic induction tomography due to patient's movement during data acquisition. *Physiological Measurement*, 30(6):S165–S174, 2009.

[78] Y. Maimaitijiang, M. A. Roula, S. Watson, R. Patz, R. J. Williams, and H. Griffiths. Parallelization methods for implementation of a magnetic induction tomography forward model in symmetric multiprocessor systems. *Parallel Computing*, 34(9):497 – 507, 2008.

[79] Y. Maimaitijiang, M. A. Roula, S. Watson, G. Meriadec, K. Sobaihi, and R. J. Williams. Evaluation of parallel accelerators for high performance image reconstruction for magnetic induction tomography. *Journal of Selected Areas in Software Engineering (JSSE)*, January Edition 2011.

[80] L. Ma, R. Banasiak, and M. Soleimani. Magnetic induction tomography with high performance gpu implementation. *Progress In Electromagnetics Research B*, 65:49–63, 2016.

[81] A. Hunt. Weighing without touching: Applying electrical capacitance tomography to mass flowrate measure in multiphase flows. *Measurement and Control*, 47(1):19–25, 2014.

[82] W. L. Yin and A. J. Peyton. Improvement of signal to noise ratio and frame capture rate in magnetic inductance tomography (mit) by exploiting transient process analysis. In *IEEE International Workshop on Imaging Systems and Techniques*, pages 239–241, 11-12 May 2009.